Editors' Suggestion

Competition between dynamic resonance and internal conversion in strong-field molecular ionization with chirped ultrafast laser pulses

Brian Kaufman,[1] Tamás Rozgonyi,[2,3] Philipp Marquetand,[4,5,6] and Thomas Weinacht[1]

[1]*Department of Physics and Astronomy, Stony Brook University, Stony Brook, New York 11794-3800, USA*

[2]*Wigner Research Centre for Physics, P.O. Box 49, H-1525 Budapest, Hungary*

[3]*Research Centre for Natural Sciences, Magyar Tudósok krt. 2, H-1117 Budapest, Hungary*

[4]*University of Vienna, Faculty of Chemistry, Institute of Theoretical Chemistry, Währinger Str. 17, 1090 Wien, Austria*

[5]*Vienna Research Platform on Accelerating Photoreaction Discovery, University of Vienna, Währinger Str. 17, 1090 Wien, Austria*

[6]*University of Vienna, Faculty of Chemistry, Data Science at Uni Vienna, Währinger Str. 29, 1090 Wien, Austria*

(Received 22 November 2020; accepted 15 January 2021; published 15 February 2021)

We show how the time-varying phase or frequency of a chirped strong-field ultrafast laser pulse can be used to control the ionization yield to different ionic states in a polyatomic molecule. The control is based upon a competition between multiphoton resonance and internal conversion. The multiphoton resonance is facilitated by dynamic Stark shifts, while the internal conversion (coupling between electronic states) is due to violation of the Born-Oppenheimer approximation. Our measurements are compared with and interpreted in terms of calculations of the strong-field ionization dynamics, which include multiphoton resonance, dynamic Stark shifts, as well as vibrational dynamics and internal conversion during the ionization process. The measurements and calculations illustrate how the light matter coupling can compete with the coupled motions of electrons and nuclei in strong-field laser-molecule interactions.

DOI: 10.1103/PhysRevA.103.023108

I. INTRODUCTION

Nonadiabatic dynamics involving the coupled motion of electrons and nuclei play an extremely important role in the photophysics of most molecules [1–8]. They are responsible for, e.g., the photoprotection of DNA and RNA bases, and are key to light harvesting, energy conversion, and the photophysics of vision [9–16]. The coupling of the electronic and nuclear degrees of freedom arises from terms in the molecular Hamiltonian that violate the Born-Oppenheimer approximation and reflect the fact that the electrons cannot adiabatically follow all nuclear motion.

Similar to the notion of adiabaticity with regard to the motion of electrons following nuclei, one can consider the adiabaticity of electrons following the variation of an applied electric field. If the frequency of an applied electric field is far from electronic resonance, the electrons in a molecule can follow the oscillations of the field adiabatically, leading to a parametric response in which the initial and final states of the molecule (before and after the application of a pulsed field) remain the same. However, if the applied field comes into resonance, then the electrons in the molecule cannot follow the field adiabatically, and the nonadiabatic dynamics that ensue lead to a change of electronic state, just as nonadiabaticity in the coupling between electrons and nuclei can lead to transitions between electronic states. Here we consider a competition between these two types of nonadiabatic electron dynamics in the resonance-enhanced strong-field ionization of a polyatomic molecule. We drive the molecules with a chirped ultrafast laser pulse whose frequency varies with time. The strong field of the laser pulse can drive Stark-shifted multiphoton resonance enhancement of the ionization [17–21], with the chirp of the pulse determining exactly when the multiphoton resonance occurs in the pulse [22].

The multiphoton resonant enhancement leads to population transfer to an excited state of the molecule, where nonadiabatic dynamics arising from electron-nuclear coupling lead to internal conversion during the ionization. We show that the chirp of the pulse can control the competition between these two types of nonadiabatic dynamics, leading to different states of the molecular cation via resonance-enhanced ionization.

In earlier work we demonstrated coherent control over the nonadiabatic electron-nuclear dynamics [23]. In this work, the control is instead focused on the nonadiabatic electron-field dynamics. Combined, the two experiments demonstrate control over the coupled field-nuclei-electron dynamics. Our measurements are interpreted in detail with calculations of the strong-field laser-molecule interaction, which solve the time-dependent Schrödinger equation with both the nuclear dynamics and the ionization included.

II. EXPERIMENT

We use an amplified Ti:sapphire laser system generating 1-mJ transform-limited pulses of 30-fs duration, centered at a wavelength of 780 nm and operating at a 1 kHz repetition frequency. Using supercontinuum generation in an argon gas cell, the pulses are spectrally broadened, producing a slightly blueshifted spectrum with a central wavelength of 750 nm and a spectrum extending from 600 to 900 nm [24–26]. Using a combination of chirped mirrors and an acousto-optic modulator (AOM) based pulse shaper, we compress the pulses to a

duration just below 10 fs [27,28]. We characterize the pulses using collinear, pulse-shaper-assisted, second harmonic generation frequency-resolved optical gating [29,30].

The shaping is performed in the frequency domain by placing an AOM in the Fourier plane of a zero dispersion stretcher [31]. The shaped electric field, $\epsilon'(\omega)$, is a product of the acoustic mask created by the AOM, $M(\omega)$, and the unshaped field, $\epsilon(\omega)$: $\epsilon'(\omega) = M(\omega)\epsilon(\omega)$. We used a mask of the form

$$M(\omega) = Ae^{i\beta(\omega-\omega_0)^2} \tag{1}$$

to generate a chirped pulse with quadratic spectral phase proportional to β (with $\beta = \varphi''/2$, where φ'' is a second order coefficient for the spectral phase in a Taylor series expansion) and a controllable overall mask amplitude A. We measured the momentum-resolved photoelectron yield as a function of β.

The shaped pulses are focused in an effusive molecular beam inside a vacuum chamber with a base pressure of 1×10^{-10} torr. The CH_2IBr molecules raise the working pressure to about 6×10^{-6} torr. The molecules are ionized by the laser, which has a peak intensity of $\sim10^{13}$ W/cm^2). The electrons generated by ionization are velocity map imaged to a dual-stack microchannel plate (MCP) and phosphor screen detector using an electrostatic lens. The electrostatic lens maps the electron velocity to position, and the light emitted by the phosphor screen at each position is recorded by a complementary metal oxide semiconductor (CMOS) camera. A fast algorithm is used to identify the coordinates $[x, y]$ of each electron hit. At these centroided positions we construct a Gaussian with a width approximately the same as the size of each hit (typically 2–3 pixels in each dimension). These Gaussians are summed to construct a synthetic VMI image free of background and detector nonuniformities. By inverse-Abel transforming and angularly integrating the two-dimensional image, we can reconstruct the three-dimensional momentum distribution of the outgoing electrons and the photoelectron spectrum.

We measured the photoelectron spectrum (PES) as a function of frequency chirp or quadratic spectral phase (linear temporal variation of the instantaneous frequency). A chirp causes the frequencies that make up the laser spectrum to arrive at different times, where a positive chirp leads to increasing frequency with time or low frequencies (red) arriving before high frequencies (blue), and a negative chirp leads to decreasing frequency or high frequencies arriving before low ones. In the resulting PES shown in Fig. 1, we see two peaks (indicated by the diagonal dashed black lines) assigned to ionic states D_3 (in the region from about 0 to 0.4 eV) and D_1 (in the region from about 0.6 to 0.9 eV). These assignments are based on previous measurements [23,32,33]. We note that the time variation of the instantaneous frequency leads to a shift in the peak positions for positive vs negative chirp. This shift occurs because ionization follows resonant excitation, and since different chirps lead to different photon energies toward the end of the pulse, the electron will be emitted with different photoelectron energies. However, the most striking feature of the PES is the asymmetry between positive and negative chirps, with the D_3 signal only for positive chirps.

While different chirps lead to different peak intensities for a constant pulse energy, equal and opposite chirps have the same intensity profiles, and thus the difference in the ionization dynamics is driven by the frequency variation of the field rather than by any intensity differences. This motivates a more detailed comparison of the photoelectron spectrum for equal but opposite chirps. Figure 2 shows photoelectron spectra for chirps of ±105 fs^2 taken from Fig. 1. These lineouts are smoothed by averaging with their nearest neighbors. For the positive chirp in red we see the D_1 peak at 0.8 eV with a D_3 peak between 0.2 and 0.35 eV. However, the negative chirp in blue lacks a clear D_3 peak, only showing the D_1 peak shifted to 0.65 eV. In previous work [23,32–36], we determined that these ionic states, D_1 and D_3, are correlated to neutral states which involve excitation of HOMO-1 and HOMO-3 electrons to Rydberg orbitals, labeled R_1 and R_3, respectively. It is dynamics on these neutral states during the ionization dynamics which lead to the chirp-dependent yield to D_1 and D_3.

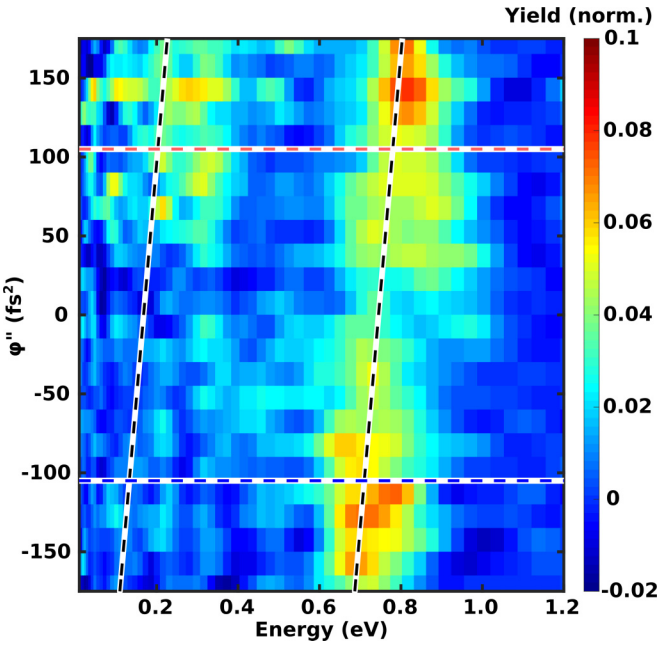

FIG. 1. Photoelectron spectra for strong-field ionization of CH_2BrI as a function of second-order spectral phase (chirp). Diagonal dashed black lines highlight the states of interest D_1 around 0.7 eV and D_3 around 0.2 eV. Horizontal dashed lines note energy lineouts for two chirps of the same magnitude ($\varphi = 105$ fs^2) but opposite sign where the red (light gray) line notes the positive chirp and the blue (dark gray) line the negative.

III. CALCULATIONS

In order to understand how the timing of resonance for the neutral states influences the yield to different ionic states, we carried out calculations that solved the time-dependent Schrödinger equation for a model system that includes multiphoton coupling, a discretized ionization continuum, vibrational dynamics in one dimension, and coupling between intermediate neutral states. We used the model described in Ref. [32] but excluded the states that were not relevant, R_0 and D_0, for the pulse shapes we consider here. We performed calculations for the same parameters as used in the previous calculations, and also carried out calculations for different Stark and ponderomotive shifts in order to test the robustness

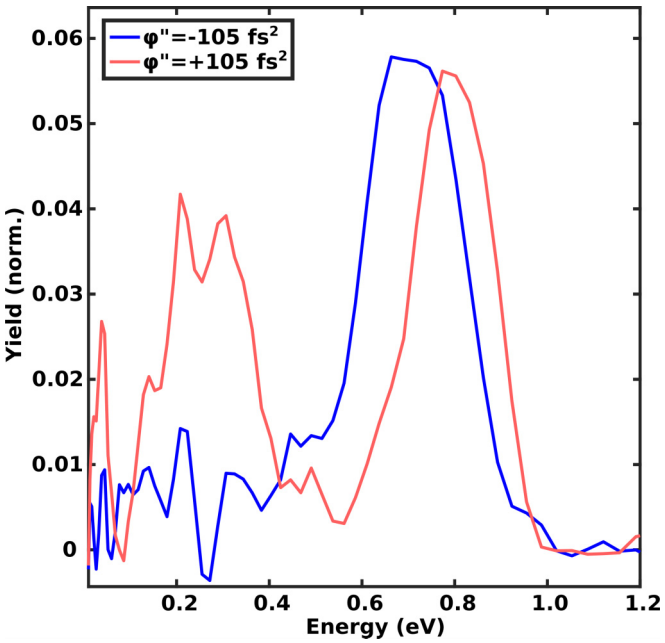

FIG. 2. Energy lineouts from Fig. 1 at horizontal dashed red-white and blue-white lines (± 105 fs^2). As before, the red (light gray) line shows the photoelectron spectrum for a pulse with a positive chirp, and the blue (dark gray) line the photoelectron spectrum for a pulse with a negative chirp. The yield is an average of the nearest neighbors and is normalized to the total number of electrons.

of the calculations. Variations in these parameters did not lead to significant changes in the molecular dynamics driven by the pulse shapes that we considered. Here we present simulations with reduced Stark shifts, no ponderomotive shifts, and no $S_0 \rightarrow R_3$ coupling for the simplest interpretation. The calculations use grid-based one-dimensional wave-packet dynamics simulations, where the potentials were obtained as harmonic fits for selected states along the CH_2 wagging mode (coordinate u). Here we describe only the equation of motion for the nuclear dynamics and the ionization process. The details of the quantum chemical computations providing the potential energy curves can be found in the electronic supporting information of Ref. [32]. The selected states consist of the neutral ground state, labeled S_0, two Rydberg states, labeled R_1 and R_3, and two cationic states, labeled D_1 and D_3. The naming for the cationic states is derived from their predominant doublet character (D_0 and D_2 are omitted here since they do not play a significant role in the measurements). The Rydberg states are Dyson correlated to the cationic state with the same index, e.g., R_1 can be ionized only to D_1. Ionization is treated by expanding the wave functions $\Psi_\alpha^{\text{ion}}(E,u,t)$ of ionic state D_α in terms of Legendre polynomials $P_l(E)$ of E as [37–39]

$$\Psi_\alpha^{\text{ion}}(u,E,t) = \sum_{l=0}^{M\to\infty} \Phi_{l+1}^{(\alpha)}(u,t)\sqrt{\frac{2l+1}{E_{\max}}}P_l\left(\frac{2E}{E_{\max}}-1\right)$$
$$\text{with} \quad \alpha = D_1, D_3, \tag{2}$$

where E is the kinetic energy of the emitted electrons, M is the maximum number of polynomials (here $M = 50$), and $E_{\max}$ is the maximally allowed kinetic energy of a photoelectron (here $E_{\max} = 2$ eV). The neutral-to-ionic multiphoton couplings $\chi_{j\alpha}(t)$ are independent of the kinetic energy E for $E < E_{\max}$ and are zero otherwise.

TABLE I. State parameters. Parameters of the different harmonic potentials used in the model simulations and the associated Stark shifts (SS) for those states for a reference of 12.78 TW/cm^2 at which our measurements were calibrated.

State	$E_{\min}$ [THz]	$u_{\min}$ [a.u.]	ω_{harm}[cm^{-1}]	SS [THz]
S_0	0	0	1200	0
R_3	1850	0.15	1260	100
R_1	1910	−0.15	1130	100
D_1	2450	−0.15	1130	–
D_3	2630	0.15	1260	–

The Rydberg states and the ionic states are populated from the ground vibrational state S_0 by multiphoton transitions, which are derived via adiabatic elimination [39–41], where the effect of off-resonant states that mediate multiphoton transitions is reproduced in the form of Rabi frequencies χ. In addition, population transfer is possible between Rydberg states by nonadiabatic couplings. The equations of motion take the following form:

$$\begin{aligned}
i\hbar\dot{\Psi}_g &= [\hat{T} + V_g(u)]\Psi_g + \sum_e \chi_{eg}^*(t)\Psi_e \\
i\hbar\dot{\Psi}_e &= \left[\hat{T} + V_e(u) + \omega_e^{(s)}(t)\right]\Psi_e + \chi_{eg}(t)\Psi_g \\
&\quad + \sum_{e'\neq e} V_{e,e'}\Psi_{e'} + \sum_\alpha \chi_{\alpha e}^*(t)\Phi_1^{(\alpha)} \\
i\hbar\dot{\Phi}_1^{(\alpha)} &= \left[\hat{T} + V_\alpha^{\text{ion}}(u) + \frac{E_{\max}}{2} + U_p(t)\right]\Phi_1^{(\alpha)} \\
&\quad + \frac{1}{\hbar}\rho_2\Phi_2^{(\alpha)} + \sum_e \chi_{\alpha e}(t)\Psi_e \\
i\hbar\dot{\Phi}_k^{(\alpha)} &= \left[\hat{T} + V_\alpha^{\text{ion}}(u) + \frac{E_{\max}}{2} + U_p(t)\right]\Phi_k^{(\alpha)} \\
&\quad + \rho_k\Phi_{k-1}^{(\alpha)} + \rho_{k+1}\Phi_{k+1}^{(\alpha)}\,.
\end{aligned} \tag{3}$$

In the above equations $\Psi_g(u,t)$ is the vibrational wave function in the ground electronic state S_0 of the neutral molecule, and $\Psi_e(u,t)$ is the wave function of the resonant neutral excited states R_e. The ρ_k's are constants defined as $\rho_k = \frac{(k-1)E_{\max}}{2\sqrt{4(k-1)^2-1}}$. $U_p(t)$ is the ponderomotive potential. In atomic units, $U_p(t) = \frac{1}{4\omega_0^2}I$, where I is the intensity of the laser pulse and ω_0 is the central laser frequency. $\hat{T}$ is the kinetic energy operator, where a reduced mass of 1.1 a.m.u. is employed, $V_e(u)$ is the diabatic potential energy curve of neutral electronic state R_e, and $V_\alpha^{\text{ion}}(u)$ is the potential energy curve (i.e., the field-free ionization potential) of ionic state D_α. All potentials are harmonic and of the form $V = \frac{1}{2}\omega_{\text{harm}}(u-u_{\min})^2 + E_{\min}$ and the corresponding parameters can be found in Table I.

$V_{e,e'}$ stand for the nonadiabatic coupling term between Rydberg states e and e', approximated by a Gaussian spatial profile centered at the crossing between the corresponding

TABLE II. Molecular couplings. Amplitudes of the multiphoton couplings (χ_{nm}) in THz for a reference of 12.78 TW/cm^2 at which our measurements were calibrated. Strength, width, and center of the nonadiabatic coupling Gaussian spatial profile.

Transition	χ_{ge}	Transition	$\chi_{e\alpha}$
$S_0 \rightarrow R_1$	20	$R_1 \rightarrow D_1$	20
$S_0 \rightarrow R_3$	0	$R_3 \rightarrow D_3$	20
NAC Transition	Strength	Width	Center
$R_1 \rightarrow R_3$	20	0.6 a.u.	–0.43 a.u.

diabatic potentials located at -0.43 a.u. for the $R_1 \rightarrow R_3$ crossing. The amplitude of the coupling was set to 20 THz, and its FWHM was set to $u = 0.6$ a.u., where u represents the vibrational normal mode coordinate. $\omega_e^{(s)}(t)$ denotes the dynamic Stark shift of the neutral excited state R_e and is set to 100 THz for both R_1 and R_3. The Stark shift of the ionic states is set to zero.

We make a multiphoton equivalent of the Condon approximation, approximating that the Rabi frequencies are independent of vibrational coordinates, i.e., the multiphoton couplings, $\chi_{jm}(t)$, have the form of $\chi_{jm}(t) = \chi_{jm}^{(0)}[\varepsilon(t)e^{-i\omega_0 t}]^{N_{jm}}$, where $\chi_{jm}^{(0)}$ is a constant parameter, and $\varepsilon(t)$ is the slowly varying envelope of the real electric field $\epsilon(t)$. The laser pulse is defined as

$$\epsilon(t) = \tfrac{1}{2}[\varepsilon(t)e^{-i\omega_0 t} + \varepsilon^*(t)e^{+i\omega_0 t}], \tag{4}$$

and based on our experimental parameters, we used a central frequency, $\omega_0 = 400$ THz, peak intensity of 12 TW/cm^2, and a Guassian envelope with a field FWHM of 14 fs for an unchirped pulse. The chirp of the pulse is considered in the simulations according to Eq. (1), with a quadratic spectral phase being applied to the pulse in the frequency domain, resulting in a variation in chirp but a constant spectral content. The N_{jm} is the photon order of the $j \rightarrow m$ transition. In our model we have $N_{ge} = 5$ and $N_{e\alpha} = 2$. The different parameters are given in Table II for an experimentally measured reference intensity of 12.78 TW/cm^2. These parameters were used for calculations that were compared with earlier experimental measurements (e.g., [32]) and made use of other experimental data, like the ionization potential of 9.69 eV [42]. The fact that the same parameters work for describing a very different set of experiments reported in this work provides further support for the model.

The results of these calculations for a ± 105 fs^2 chirp are displayed in Fig. 3, where we show the neutral and ionic state populations as a function of time. Starting with the neutral state populations in the upper panel we see that there is a delay in time between populating R_1 and R_3, which comes from the fact that R_3 can only be populated via R_1 through the nonadiabatic coupling (NAC). Focusing on R_1, we see that the population rises earlier for the positive chirp (red), with a maximum rate at around -4 fs as opposed to about 6 fs for the negative chirp (blue). These few femtoseconds are important because they give the wave packet on R_1 more time to evolve to R_3 before ionizing. Populating R_1 early with a positively

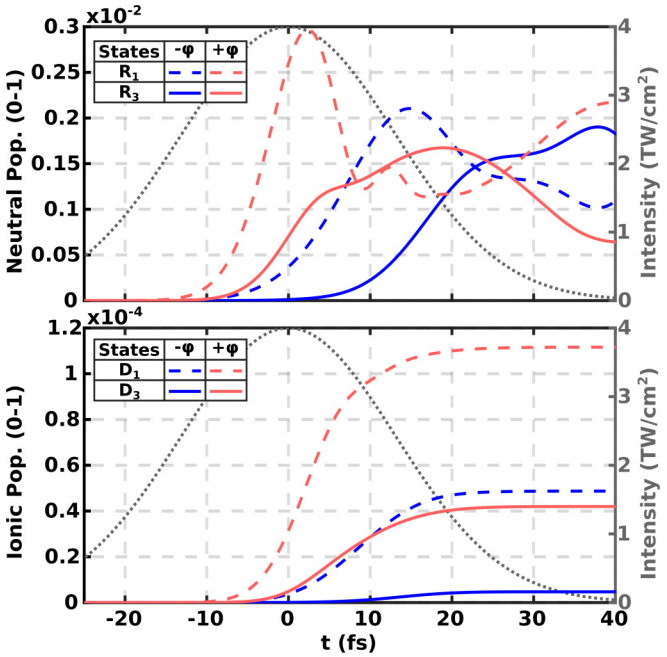

FIG. 3. Colored (solid and dashed) lines show populations as a function of time for the neutral (top panel) and ionic (bottom panel) states. Dashed lines correspond to R_1 (neutral) and D_1 (ionic), which are Dyson correlated, while solid lines correspond to R_3 (neutral) and D_3 (neutral). Blue (dark gray) lines show the populations for a negative chirp ($\varphi = -105$ fs^2), and red (light gray) lines show the positive chirp case ($\varphi = +105$ fs^2). The dotted gray line in each panel shows the intensity envelope for this chirp and corresponds to the right y axis.

chirped pulse leads to significant internal conversion before the end of the pulse, whereas populating R_1 later for a negatively chirped pulse leads to internal conversion only as the pulse is turning off. For the ionic state populations in the lower panel, we see that significant ionization to D_3 only takes place if R_3 is populated before the pulse turns off. The calculations are in agreement with the experimental results: only the positive chirp shows significant ionization to D_3.

For a more quantitative comparison of experiment and theory, Fig. 4 shows the D_3/D_1 ratio as a function of chirp. The simulated ratio is calculated from the final ionic state populations of D_1 and D_3 for calculations performed with the same intensity envelope, as expected in the experiment. The experimental ratio was calculated by integrating the D_1 and D_3 peaks in the PES of Fig. 1. While the measurements and calculations show the same behavior for the D_3/D_1 ratio as a function of chirp, the magnitude of the ratio is different. There are a number of parameters/factors in the calculations that could account for the difference. These include not accounting for focal volume averaging of the laser intensity, the strengths of the multiphoton Rabi frequencies, and the strength of the nonadiabatic coupling between R_1 and R_3. Furthermore, the background subtraction in the experiments (electrons arising from nonresonant multiphoton or tunnel ionization) can have a significant effect on the magnitude of the D_3/D_1 ratio. While the magnitude of the D_3/D_1 ratio can be sensitive to these aspects of the calculations and measurements, the variation

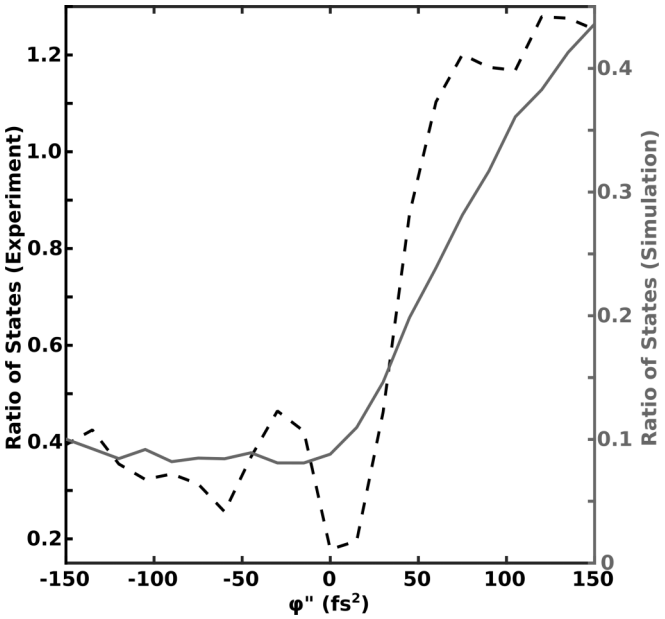

FIG. 4. Comparison of the measured and simulated D_3/D_1 ratio. The dashed black line shows the experiment and corresponds to the left *y* axis, while the solid gray line shows the simulation and corresponds to the right *y* axis.

in the D_3/D_1 ratio with chirp is relatively insensitive to these issues, allowing for a meaningful comparison between experiment and simulation.

IV. DISCUSSION

Figure 5 illustrates how positively and negatively chirped laser pulses drive differences in the strong-field ionization yield of CH_2IBr. The left panel shows the Stark-shifted state energy of R_1 as a function of time. It follows the laser intensity profile for the chirped pulse. The color ordering of the linear frequency chirps is shown by the red (positive chirp) and blue (negative chirp) lines which show the instantaneous energy associated with the five-photon absorption ($5h\nu$) as a function of time. One can see that the laser comes into resonance with the Stark-shifted state around -10 fs for a positive frequency chirp, which is well before the case for a negative frequency chirp (around 10 fs). The right panel shows the potential energy curves for the relevant neutral states as a function of CH_2 wagging displacement at -10 fs. The vertical arrows show the instantaneous five photon energy of the laser for a positive (red) and negative (blue) chirp. One can see that a positively chirped pulse is resonant and can excite a wave packet to R_1 (green), which can nonadiabatically couple to R_3 during the remainder of the pulse, while a negatively chirped pulse is not resonant early in the pulse and does not transfer population to R_1 at this time. The early resonance for positive chirp allows for population of R_1 on the rising edge of a positively chirped pulse, which can then be followed by internal conversion to R_3 and ionization to both D_1 and D_3. For a negatively chirped pulse, the multiphoton resonance takes place much later, and thus while there is ionization to D_1, there is insufficient time during the remainder of the pulse for internal conversion to R_3 and ionization to D_3.

This picture explains the measurements, which show that ionization to D_3 depends strongly on chirp, with positive chirps producing substantial D_3 (particularly between 70 and 170 fs^2) and negative chirps producing negligible D_3. This simple interpretation leads to two simple predictions. One is that the effect should be most pronounced for low intensities where R_3 just barely comes into resonance, and the other is that the location of the D_1 peak should shift with chirp,

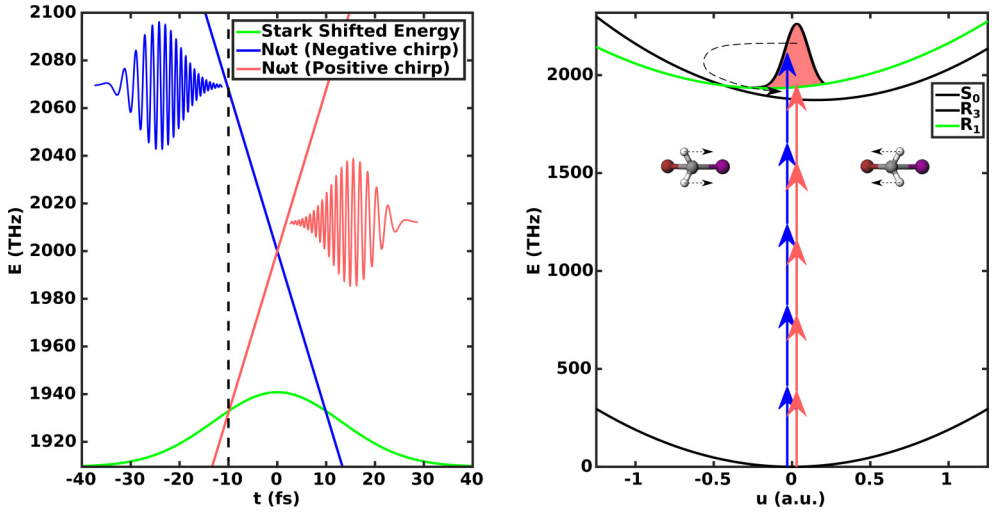

FIG. 5. Illustration of how positively and negatively chirped laser pulses drive differences in the strong-field ionization yield of CH_2IBr. The left panel shows the time-dependent R_1 energy (green), along with the energy of five photons for a positively (red-light gray) and negatively (blue-dark gray) chirped pulse. Red and blue cartoons of the electric fields are included to visualize the chirps. The right panel shows the relevant potential energy curves as a function of the CH_2 wagging displacement (u). The blue and red arrows illustrate the instantaneous photon energy at the time corresponding to the dashed vertical black line in the left-hand panel. A wave packet is excited by the positive chirp (red arrows) and evolves through the conical intersection connecting the states R_1 (green) and R_3 (upper black). A cartoon of the molecule is shown with arrows indicating the CH_2 wagging.

reflecting the instantaneous frequency of the laser during ionization from R_1 to D_1. Both of these two predictions are born out in our measurements. Measurements for higher pulse energies show a much less pronounced chirp dependence for the ionization to D_3, and one can see the expected shift in the D_1 peak in the PES with chirp, of about 0.1 eV, which is consistent with a $\sim$ 40-THz shift in the average frequency of the square of the field associated with two-photon ionization from R_1 to D_1.

V. CONCLUSION

In conclusion, we present and interpret the strong-field ionization of CH_2IBr with chirped ultrafast laser pulses. The measurements are interpreted in terms of a competition between multiphoton resonance and internal conversion. The multiphoton resonant enhancement leads to population transfer to an excited state of the molecule, which can be considered as a nonadiabatic response of the electrons to the laser pulse. Nonadiabatic dynamics on this excited state arising from electron-nuclear coupling can then lead to internal conversion to an additional electronic state. Depending on the timing of the resonance, the molecule may or may not have enough time to undergo this internal conversion before ionization to different states of the molecular cation. These results can be seen as a competition between two different types of nonadiabatic dynamics.

ACKNOWLEDGMENTS

This work was supported by the National Science Foundation under Award No. 1806294. It was also partly supported by the Government of Hungary and the European Regional Development Fund under Grant No. VEKOP-2.3.2-16-2017-00015.

[1] S. Matsika and A. I. Krylov, Chem. Rev. **118**, 6925 (2018).
[2] T. J. Martínez, Acc. Chem. Res. **39**, 119 (2006).
[3] M. Barbatti, B. Sellner, A. J. A. Aquino, and H. Lischka, in *Radiation Induced Molecular Phenomena in Nucleic Acids*, edited by M. Shukla and J. Leszczynski, Challenges and Advances in Computational Chemistry and Physics Vol. 5 (Springer, Netherlands, 2008), pp. 209–235.
[4] J. E. Subotnik, A. Jain, B. Landry, A. Petit, W. Ouyang, and N. Bellonzi, Annu. Rev. Phys. Chem. **67**, 387 (2016).
[5] B. F. E. Curchod and T. J. Martínez, Chem. Rev. **118**, 3305 (2018).
[6] M. Vacher, I. Fdez. Galván, B.-W. Ding, S. Schramm, R. Berraud-Pache, P. Naumov, N. Ferré, Y.-J. Liu, I. Navizet, D. Roca-Sanjuán *et al.*, Chem. Rev. **118**, 6927 (2018).
[7] J. Westermayr and P. Marquetand, Chem. Rev. (2020).
[8] L. González and R. Lindh, *Quantum Chemistry and Dynamics of Excited States: Methods and Applications* (John Wiley and Sons Ltd., New York, 2020).
[9] T. Mirkovic, E. E. Ostroumov, J. M. Anna, R. van Grondelle, Govindjee, and G. D. Scholes, Chem. Rev. **117**, 249 (2017).
[10] T. R. Nelson, A. J. White, J. A. Bjorgaard, A. E. Sifain, Y. Zhang, B. Nebgen, S. Fernandez-Alberti, D. Mozyrsky, A. E. Roitberg, and S. Tretiak, Chem. Rev. **120**, 2215 (2020).
[11] T. Schultz, E. Samoylova, W. Radloff, I. V. Hertel, A. L. Sobolewski, and W. Domcke, Science **306**, 1765 (2004).
[12] W. J. Schreier, T. E. Schrader, F. O. Koller, P. Gilch, C. E. Crespo-Hernández, V. N. Swaminathan, T. Carell, W. Zinth, and B. Kohler, Science **315**, 625 (2007).
[13] C. Rauer, J. J. Nogueira, P. Marquetand, and L. González, J. Am. Chem. Soc. **138**, 15911 (2016).
[14] C. Rauer, J. J. Nogueira, P. Marquetand, and L. González, Monatsh. Chem. **149**, 1 (2018).
[15] J. Herbst, K. Heyne, and R. Diller, Science **297**, 822 (2002).
[16] E. Tapavicza, I. Tavernelli, and U. Rothlisberger, Phys. Rev. Lett. **98**, 023001 (2007).
[17] R. R. Freeman and P. H. Bucksbaum, J. Phys. B **24**, 325 (1991).
[18] R. R. Freeman, P. H. Bucksbaum, H. Milchberg, S. Darack, D. Schumacher, and M. E. Geusic, Phys. Rev. Lett. **59**, 1092 (1987).
[19] G. N. Gibson, R. R. Freeman, and T. J. McIlrath, Phys. Rev. Lett. **67**, 1230 (1991).
[20] G. N. Gibson, R. R. Freeman, T. J. McIlrath, and H. G. Muller, Phys. Rev. A **49**, 3870 (1994).
[21] D. Geißler, P. Marquetand, J. González-Vázquez, L. González, T. Rozgonyi, and T. Weinacht, J. Phys. Chem. A **116**, 11434 (2012).
[22] M. Krug, T. Bayer, M. Wollenhaupt, C. Sarpe-Tudoran, T. Baumert, S. S. Ivanov, and N. V. Vitanov, New J. Phys. **11**, 105051 (2009).
[23] B. Kaufman, T. Rozgonyi, P. Marquetand, and T. Weinacht, Phys. Rev. Lett. **125**, 053202 (2020).
[24] L. Gallmann, T. Pfeifer, P. Nagel, M. Abel, D. Neumark, and S. Leone, Appl. Phys. B **86**, 561 (2007).
[25] C. Hauri, W. Kornelis, F. Helbing, A. Heinrich, A. Couairon, A. Mysyrowicz, J. Biegert, and U. Keller, Appl. Phys. B **79**, 673 (2004).
[26] F. Hagemann, O. Gause, L. Wöste, and T. Siebert, Opt. Express **21**, 5536 (2013).
[27] G. Stibenz, N. Zhavoronkov, and G. Steinmeyer, Opt. Lett. **31**, 274 (2006).
[28] M. A. Dugan, J. X. Tull, and W. S. Warren, J. Opt. Soc. Am. B **14**, 2348 (1997).
[29] R. Trebino, K. W. DeLong, D. N. Fittinghoff, J. N. Sweetser, M. A. Krumbügel, B. A. Richman, and D. J. Kane, Rev. Sci. Instrum. **68**, 3277 (1997).
[30] I. Amat-Roldán, I. G. Cormack, P. Loza-Alvarez, E. J. Gualda, and D. Artigas, Opt. Express **12**, 1169 (2004).
[31] A. M. Weiner, Rev. Sci. Instrum. **71**, 1929 (2000).
[32] P. Sándor, V. Tagliamonti, A. Zhao, T. Rozgonyi, M. Ruckenbauer, P. Marquetand, and T. Weinacht, Phys. Rev. Lett. **116**, 063002 (2016).

[33] V. Tagliamonti, B. Kaufman, A. Zhao, T. Rozgonyi, P. Marquetand, and T. Weinacht, Phys. Rev. A **96**, 021401(R) (2017).
[34] D. Geißler, T. Rozgonyi, J. González-Vázquez, L. González, P. Marquetand, and T. C. Weinacht, Phys. Rev. A **84**, 053422 (2011).
[35] V. Tagliamonti, P. Sándor, A. Zhao, T. Rozgonyi, P. Marquetand, and T. Weinacht, Phys. Rev. A **93**, 051401(R) (2016).
[36] W. Liu, J. Chem. Phys. **152**, 180901 (2020).
[37] M. Seel and W. Domcke, J. Chem. Phys. **95**, 7806 (1991).
[38] T. Rozgonyi, A. Glaß, and T. Feurer, J. Appl. Phys. **88**, 2936 (2000).
[39] W. D. M. Lunden, P. Sándor, T. C. Weinacht, and T. Rozgonyi, Phys. Rev. A **89**, 053403 (2014).
[40] M. Fewell, Opt. Commun. **253**, 125 (2005).
[41] B. Kaufman, T. Rozgonyi, P. Marquetand, and T. Weinacht, Phys. Rev. A **102**, 063117 (2020).
[42] A. F. Lago, J. P. Kercher, A. Bödi, B. Sztáray, B. Miller, D. Wurzelmann, and T. Baer, J. Phys. Chem. A **109**, 1802 (2005).